THE JOURNAL OF PHYSICAL CHEMISTRY A
A JOURNAL OF THE AMERICAN CHEMICAL SOCIETY

pubs.acs.org/JPCA Article

Vibrational Analysis Based on Cavity-Enhanced Raman Spectroscopy: Cyclohexane

Published as part of The Journal of Physical Chemistry A special issue "Alec Wodtke Festschrift".

Qing-Ying Yang,[#] Qin Yang,[#] Yi-Fan Song, An-Wen Liu, Jin Wang, Yan Tan,* Yu R. Sun, and Shui-Ming Hu*

Cite This: *J. Phys. Chem. A* 2025, 129, 3183−3193 Read Online

ABSTRACT: Cyclohexane (CAS: 110-82-7), a colorless organic solvent derived from petroleum, is a valuable reference standard for Raman shift calibration and serves as a model for six-membered ring structures in complex chemical and biological systems. In this study, we measured polarized Raman spectra of gaseous cyclohexane at room temperature using cavity-enhanced Raman spectroscopy (CERS) across the range of 200−3200 cm^{-1}. The observed vibrational wavenumbers, intensities, and depolarization ratios were compared with calculated values, enabling the assignment of several dozen Raman-active bands, including many overtone and combination bands. This work demonstrates the capability of CERS for vibrational analysis of gas-phase polyatomic molecules.

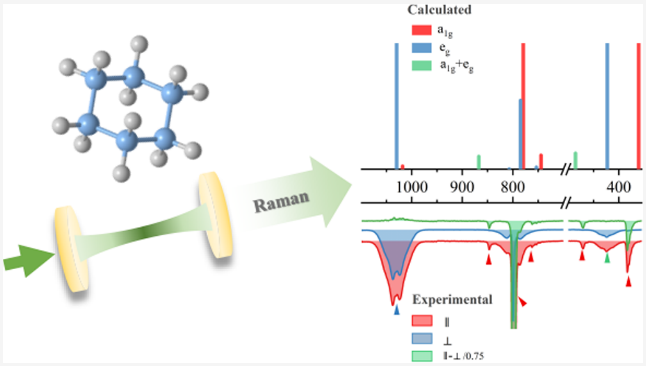

■ INTRODUCTION

Advancements in computational and experimental methodologies have significantly elevated Raman spectroscopy as a powerful analytical tool across both applied and fundamental sciences.[1] Its applications range from standard analyses of liquids and crystals in laboratory settings[2,3] to more specialized uses in areas like food quality assessment, environmental pollution monitoring with hand-held Raman devices.[4,5] Raman spectrometers are now even deployed in extreme environments, such as hydrothermal vents on the ocean floor,[6] and on remote-controlled platforms for field analyses.[7−9] Recently, Raman signals have even been detected from distant planetary surfaces via telescopic systems.[10,11]

Since the inception of laser-based Raman spectroscopy, researchers have aimed to establish a unified standard for Raman intensity measurements. Contributions by Mattioda and Yassine have advanced this goal through the development of comprehensive spectral libraries, refined data analysis techniques, and the identification of spectral variations.[12−14] Yet, analyzing Raman spectra of polyatomic molecules remains challenging due to reliance on quantum mechanical calculations for spectrum assignments, which are inherently prone to biases.[15−18] As the molecular system grows in size, accurately determining the penitential energy surface becomes significantly more difficult. Density functional theory (DFT) methods offer a practical balance between computational cost and efficiency. The development of double-hybrid DFT methods has further enhanced accuracy.[19] However, the performance of DFT is highly dependent on the choice of functionals or basis sets, making it a persistent challenge to identify combinations that are universally applicable across diverse molecular systems.[20,21] Another challenge arises from spectra simulation methods.[22] Accounting for anharmonicity is essential to interpret experimentally observed combinations and overtones, especially as experimental techniques continue to advance in sensitivity and precision. Implementing simulations at the anharmonic level is not only algorithmically complex but also computationally demanding. Comparative studies between theoretical and experimental data have addressed such challenges for various compounds, including silacyclohexane, xylenes, butane, acetonitrile, and 2-butanol.[16,17,23−25] Expanding the data set with more precise gas-phase data could enhance the accuracy and reliability of quantum models.

However, gas-phase Raman spectra acquisition is particularly difficult due to small differential Raman cross sections (around 10^{-30} cm^2 sr^{-1} molecule^{-1}), which often restricts Raman

Received: November 14, 2024
Revised: March 18, 2025
Accepted: March 20, 2025
Published: March 31, 2025

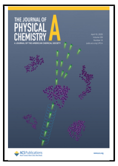

https://doi.org/10.1021/acs.jpca.4c07709
J. Phys. Chem. A 2025, 129, 3183−3193

spectroscopy to condensed-phase samples with much higher molecular densities (10^{20}−10^{22} cm^{-3}).[26−29] This change in molecular environment causes shifts in spectral lines and affects line shapes, complicating analyses.[30] For example, phase-dependent shifts and intensity variations have been observed in chlorofluorosilane Raman spectra, illustrating how molecular interactions influence spectral characteristics.[31]

Cavity-enhanced Raman spectroscopy (CERS)[32−37] has recently emerged as a promising technique to obtain high-precision spectral data for gas-phase molecules, significantly improving the accuracy of vibrational assignments. The sensitivity is considerably enhanced by the high intracavity laser power of hundreds of Watts. A pulsed laser may also achieve such a power, but its high peak power can easily induce a fluorescence background due to multiphoton effects. Meanwhile, it is not a problem for CERS based on continuous-wave lasers. In this study, we employ polarized Raman spectroscopy to investigate polyatomic molecules, including polarization measurements that yield depolarization ratios. These ratios, indicating the symmetry of vibrational modes, aid in vibrational assignments and molecular structure determination.[38−40] Additionally, this technique can distinguish enantiomers in chiral media and reduce background interference.[25,33]

The ultimate goal of studies in this direction is to establish a comprehensive Raman spectral database to facilitate chemical quantification.[41] For demonstration, we focus on cyclohexane in this work, which is a well-known benchmark molecule for Raman study. Cyclohexane (CAS: 110-82-7) is a colorless organic solvent distilled from petroleum, commonly in liquid form at standard temperature and pressure. Short-term exposure may depress the central nervous system, while long-term exposure is associated with liver and kidney toxicity. Cyclohexane is primarily released into the atmosphere through vehicle emissions and is considered a standard for Raman shift calibration.[42,43] Previous research has extensively studied liquid cyclohexane spectra using infrared spectroscopy, Raman spectroscopy, and theoretical simulations.[18,44] Early work by Miller in the 1960s provided foundational Raman spectra for liquid cyclohexane,[45] with vibrational assignments based on infrared data from solid-phase cyclohexane.[46,47] Miller also explored cyclohexane's stereochemistry, examining its chair and boat conformations and the effects of substituted and isotopically labeled cyclohexanes on these structures.[48] Despite substantial research, Raman data for gaseous cyclohexane remains limited. In 1989, Lorenzo et al.[49] recorded the Raman spectrum of cyclohexane gas with a resolution of 5 cm^{-1}.

In this work, we present an analysis of the cavity-enhanced Raman spectra of gas-phase cyclohexane, comparing with theoretical predictions and prior experimental data. Details of the experimental setup and computational methodologies—including density functional theory (DFT) and the double hybrid DFT approach—are discussed in Section Experimental and Theoretical Methods, with results and analysis provided in Section Results and Disscusion.

EXPERIMENTAL AND THEORETICAL METHODS

CERS Measurements. We employed a cavity-enhanced Raman spectroscopy (CERS) apparatus, with the schematic configuration shown in Figure 1. The experimental setup is similar to that reported previously[37] and modifications were applied to retrieve the polarized Raman signal. A continuous-wave laser at 532 nm and up to 1 W of power output was directed through an achromatic half-wave plate and a polarizing beam splitter (PBS) with a high extinction ratio of 1000:1 for parallel (T_P) to perpendicular (T_S) polarizations. The resulting polarized light was then fed into a high-finesse optical cavity (HFC), while the light reflected by the PBS was used for PDH locking. This locking servo kept the resonance between the 532 nm laser and the 72 cm-long cavity, maintaining high intracavity power that significantly enhances the Raman signal. The mirror reflectivity has been determined to be 0.99995 by cavity ring-down measurement of an empty cavity. The mirror loss was determined to be 3×10^{-5} by measuring the transmittance of the cavity by locking the laser with the cavity. The effective circulating power inside the cavity could be calculated according to the equations given in our previous work.[37] The enhancement factor, as the ratio between the power inside the cavity and the power transmitted from the cavity, I_{cav}/I_{out}, was determined to be 50 000. During the experiment, we monitored the transmitted laser power and used its value to normalize the amplitude of the Raman signal.

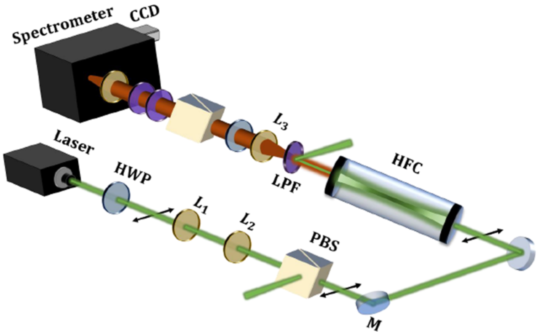

Figure 1. Schematic layout of the polarized cavity-enhanced Raman spectroscopy setup. HWP, half-wave plate; L: lenses; PBS, polarizing beam splitter; M: plane reflecting mirror; HFC: high-finesse cavity; and LPF: long-pass filter.

Inside the cavity, the light largely retained its linear polarization; however, slight degradation occurred due to stress-induced birefringence from the high-reflectivity mirror coatings. Polarization of the light exiting the cavity was assessed with and without gas samples. The extinction ratio of 1000:1 at the cavity's input decreased to 100:1 upon exiting, and further reduced to 50:1 after passing through additional optical components (e.g., lenses, mirrors, filters) before entering the grating spectrometer. A linear polarizer was used in the optical path to measure the depolarization ratio of Raman transitions.

The gas sample was introduced into the HFC, and the forward Raman scattering signal was collimated and focused onto the slit of a spectrometer (Shamrock 750, Andor) using an achromatic lens. Between two achromatic lenses along the beam path, the signal passed through an achromatic half-wave plate, optimized for 450−650 nm, and a polarizing beam splitter (PBS) with a 1000:1 transmission-to-reflection ratio for wavelengths in the 420−680 nm range, resulting in P-polarized light. Long-pass filters (BLP01-532R-25) were used to block transmitted laser light and Rayleigh-scattered light. A combination of an achromatic half-wave plate and a PBS enabled the separation of Raman-scattered light into components parallel or perpendicular to the laser polarization, allowing for polarization-resolved Raman spectra by adjusting the angle of the half-wave plate.

The spectrometer, featuring a 750 mm focal length and a 1200 grooves/mm grating, provided a spectral resolution of approximately 0.1 nm. Paired with a CCD camera (DV401A-BVF, sensitive from 200 to 1100 nm), this setup achieved a nominal spectral resolution of around 2 cm^{-1}. The spectrum was calibrated with atomic neon emission lines. The frequency accuracy was confirmed to be 3 cm^{-1} by comparing the peak positions of H_2, N_2, and O_2 with their frequencies given in the literature.[42,50]

The Raman spectrum of cyclohexane vapor was recorded under low-pressure conditions using liquid cyclohexane from Aladdin Corporation (purity >99.9%). Following liquefaction, the cyclohexane vapor pressure was maintained at approximately 8 kPa at room temperature (293 K). Vapor was injected into the cavity through a needle valve, and the cavity pressure was continuously monitored using a thin-film pressure gauge (10 kPa full scale, 0.5% accuracy) to account for potential adsorption between the vapor and the cavity walls. To ensure a high signal-to-noise ratio, multiple Raman spectra were recorded under identical conditions and averaged, with background subtraction based on the spectrum from an empty cavity. Repeating the experiment on separate days confirmed data consistency. Laser intensity was tracked using a photodiode connected to a USB oscilloscope (Picoscope 6402C), monitoring scattered light from the mirror. The photodiode was calibrated with a standard Si photodiode (S121C, Thorlabs) connected to a power meter (PM100D, Thorlabs), with a sensitivity of 10 nW. The statistical error in Raman peak intensity was approximately 5%. However, the systematic error may reach 80%, which relates to various issues, such as the laser power, wavelength-dependent efficiency, detector nonlinearity, etc. The high-finesse cavity also opposes influence on the scattering light with wavelength below 605 nm, where the cavity mirrors have a reflectivity over 99%. The influence has been quantitatively assessed in our previous work[37] and will not be repeated here. The observed Raman signal intensities below 2260 cm^{-1} may be attenuated by up to 80% due to uncorrected instrumental effects. Consequently, while the spectral features in this region remain detectable, their relative intensities should be interpreted with caution when making quantitative comparisons with distant bands.

Theoretical Method. The cyclohexane molecule exists in two conformations: chair and boat, with the chair conformation being much more stable. At room temperature, the theoretical ratio of chair-to-boat conformations is approximately 10000:1. Therefore, this work will focus exclusively on the chair conformation of cyclohexane. The chair conformation of cyclohexane (symmetry D_{3d}) has 48 normal vibration modes, corresponding 32 fundamental vibrational bands in total:[44,51] 6 a_{1g} ($\nu_1 - \nu_6$), 3 a_{1u} ($\nu_7 - \nu_9$), 2 a_{2g} (ν_{10}, ν_{11}), 5 a_{2u} ($\nu_{12} - \nu_{16}$), 8 e_g ($\nu_{17} - \nu_{24}$), and 8 e_u ($\nu_{25} - \nu_{32}$). In the gas phase, a_{2u} and e_u modes are infrared active, a_{1g} and e_g modes are Raman active, while a_{1u} and a_{2g} modes are inactive. Descriptions of the normal modes used in this work are given in Table S1 of Supporting Information (SI), and their presentations are in Figure S4.

Electronic structure calculations were performed using density functional theory (DFT) and double-hybrid DFT methods. Structure optimizations were carried out with a stringent convergence criterion, with maximum forces set to 2 $\times 10^{-6}$ Hartrees/Bohr and maximum displacements limited to 6×10^{-6} Å. The B3PW91/jun-cc-pVTZ and revDSD-PBE86-D3/jun-cc-pVTZ methods proved efficient for the vibrational spectra simulation.[21,52,53] Both methods, including their respective empirical dispersion (ED) corrections, were used for structure optimization and frequency calculation at the harmonic level. Due to the lack of incident light property calculations available with revDSD-PBE86-D3, only B3PW91/jun-cc-pVTZ was used for anharmonic simulations. Taking into account the molecular size of cyclohexane (18 atoms), a method based on the second-order vibrational perturbation theory (VPT2) is used to account the anharmonicity. Anharmonic data were derived via numerical differentiation of the analytic second derivatives of the potential energy and first derivatives of relevant properties, using a step size of 0.01 $\sqrt{\text{amu}}\cdot$Å along the mass-weighted normal coordinates.[54,55]

A hybrid method is used to get a higher accuracy, with acceptable computational cost.[21,52] In the hybrid method, the potential energy surface and harmonic force constants were taken from revDSD-PBE86-D3/jun-cc-pVTZ, while the anharmonic force constants and properties were computed using B3PW91/jun-cc-pVTZ. jun-cc-pVTZ provides balanced computational cost and efficiencies, and it have been testified for the anharmonic study.[52,56,57] The consistency of normal modes between these two levels was verified through the Duschinsky transformation,[58−60]

$$\mathbf{Q}^H = \mathbf{J}\mathbf{Q}^L + \mathbf{K} \tag{1}$$

where $\mathbf{Q}^H$ represents the mass-weighted normal coordinates at the higher-level ESCM (revDSD-PBE86-D3/jun-cc-pVTZ), $\mathbf{Q}^L$ from the lower-cost method (B3PW91/jun-cc-pVTZ), $\mathbf{J}$ is the Duschinsky matrix, and $\mathbf{K}$ is the shift vector of the two sets of normal modes.

Combination and overtone transitions were considered up to three quanta.[61] An intensity-specific generalized VPT2 (GVPT2) scheme[55,62,63] was used to identify resonances, employing automatized procedures for resonance detection. At the end of the resonance analysis procedure, a variational process was applied to reintroduce the terms that were being deleted due to resonances.[52] Detailed resonance information is provided in the SI.

Conformer analysis of hexane is provided in the SI. All optimizations, frequency calculations, and anharmonic force field evaluations were conducted using Gaussian 16 (G16). Resonances analysis and final Raman intensity calculations were performed with a locally modified version of G16. Custom scripts were developed for data analysis and spectral plotting, with the final results represented by Gaussian distributions with a half-width at half-max (HWHM) of 2 cm^{-1}.

■ RESULTS AND DISSCUSION

Experimental Results. Figure 2 presents the normalized Raman spectra of cyclohexane across the range of 200−3200 cm^{-1}, recorded at room temperature. The spectra were collected with an integration time of 1 s and a laser power of 3 mW transmitted from the cavity, corresponding to an intracavity power of approximately 150 W. The initial gas pressure inside the cavity was 1 kPa. Figure 2a,b show the Raman spectra for the parallel and perpendicular polarization components, respectively. The depolarization ratio (ρ) for each peak was calculated as the ratio of the perpendicular component's intensity to that of the parallel component. The observed vibrational bands can be assigned based on their

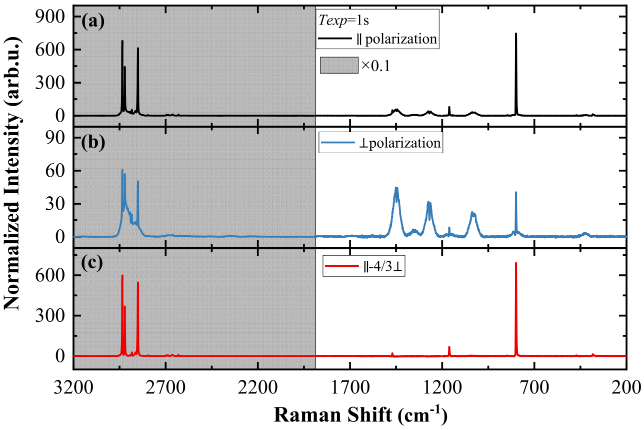

Figure 2. Polarized Raman spectra of cyclohexane spanning the 200−3200 cm^{-1} range: (a) Raman spectrum with parallel laser polarization; (b) Raman spectrum with perpendicular laser polarization; (c) isotropic component of the Raman spectrum, $I_i = I_{\parallel} - \frac{4}{3}I_{\perp}$. Note that the data shown in the shadow region have been multiplied by a factor of 0.1.

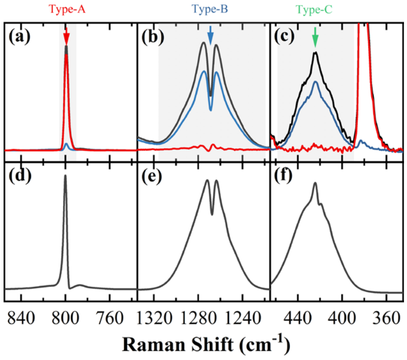

Figure 3. Three different shapes of the Raman bands of gaseous cyclohexane. (a) Polarized ν_5 band at 799 cm^{-1}. This band has a characterized narrow Q peak and a depolarization ratio of nearly 0. (b) Polarized ν_{21} band at 1268 cm^{-1}. This band is characterized by a splitting band center and a depolarization ratio of 0.75. (c) Polarized ν_{24} band around 424 cm^{-1}. This band has a narrow peak on top of a broad feature. The depolarization ratio is 0.75. (d) Type-A band: Simulated profile of a parallel Raman band with rotational transitions of $\Delta K = 0$, $\Delta J = 0, \pm1, \pm2$. Note that those transitions with $\Delta J = \pm1, \pm 2$ have a depolarization ratio of 0.75. (e) Type-B band: Simulated profile of a perpendicular Raman band with rotational transitions of $\Delta K = \pm1, \pm2$, $\Delta J = 0, \pm1, \pm2$. (f) Type-C band: Simulated profile of a perpendicular band with rotational transitions of $\Delta K = \pm1, \pm2$, $\Delta J = 0, \pm1, \pm2$, together with a peak at the center due to Coriolis interaction. Ground state spectroscopic constants, $B = 0.1436354$ cm^{-1}, $C = 0.0821682$ cm^{-1}, $D_J = 3.126 \times 10^{-8}$ cm^{-1}, $D_{JK} = -4.576 \times 10^{-8}$ cm^{-1}, and the Coriolis coupling coefficient of -6.68×10^{-3} cm^{-1}, were used to simulate the band shape.[44]

corresponding frequencies, intensities, and depolarization ratios.

The Raman spectrum consists of both polarized (I_i) and depolarized (I_a) components. The depolarized component, corresponding to the intensity of the perpendicular Raman scattering radiation ($I_{\perp}$), is expected to have a depolarization ratio of 0.75 relative to the parallel Raman scattering intensity ($I_{\parallel}$). The polarized component could be derived using the following equation:

$$I_i = I_{\parallel} - \frac{4}{3}I_{\perp} \tag{2}$$

We have verified the depolarization ratio ρ obtained in this work by measuring the rotation-resolved Raman bands of N_2, O_2, and CO_2 in the range of 1250−2550 cm^{-1}. For a well-isolated band, the uncertainty of ρ derived from the experiment was estimated to be about 0.05, and no wavelength dependence was observed. Figure 2c shows an overview of the polarized part of the Raman spectrum of cyclohexane.

The gas-phase polarized Raman spectra of cyclohexane reveal three distinct profiles, labeled type-A, B, and C, as depicted in Figure 3a−c, respectively. The arrows indicate the positions of the fundamental bands ν_5, ν_{21}, and ν_{24}. The red curves in the figure represent the results obtained by subtracting the vertical polarization signal (blue curves) divided by 0.75 from the parallel polarization signal (black curves). Importantly, by linearly subtracting the perpendicular Raman spectrum from the parallel spectrum, we can isolate the narrow isotropic component from overlapping spectral features. Further examples will be given below to illustrate this approach.

The ν_5 (a_{1g}) band of type-A shown in Figure 3a has a very narrow width of about 4 cm^{-1} and a depolarization ratio close to zero. According to the selection rules for Raman spectra,[64] for the polarized $a_{1g} - a_{1g}$ Raman band of a D_{3d} molecule, a sharp characterized Q branch with rotational transitions of $\Delta K = 0$, and $\Delta J = 0$ occurs at the band center. A simulated spectrum is shown in Figure 3d. In the simulation, we used the rotational population intensity distribution according to the rotational parameters from the literature[44] and Placzek-Teller Factors for symmetric top molecules. The Q branch has a depolarization ratio of zero and disappears in the spectrum with perpendicular polarization. Note that rotational transitions with $\Delta J = \pm 1, \pm 2$ in this band can also be observed, which spread around the band center and exhibit a depolarization ratio of 0.75. These depolarized lines result in a nonzero depolarization ratio derived from the observed spectrum. Note that here we just gave a simulation with a resolution of 1 cm^{-1} compatible with the experimental resolution. The rotational structures could be resolved in high-resolution measurements. The ν_{21} (e_g) and ν_{24} (e_g) bands, shown in Figure 3b,c, both exhibit broad profiles covering over 40 cm^{-1} and have a depolarization ratio of 0.75. In the framework of the selection rule applied to degenerate Raman bands of molecules with D_{3d} symmetry,[64] transitions with $\Delta K = \pm1$ and $\Delta K = \pm2$ are allowed for $e_g - a_{1g}$ Raman bands. A simulated band profile incorporating rotational transitions of $\Delta K = \pm 1$ and $\Delta K = \pm 2$ is presented in Figure 3e. The broad spectral feature arises from a series of Q branches distributed over a wide range, with a narrow dip located at its center. The simulated profile closely matches the observed type-B spectrum shown in Figure 3b. As discussed by Herzberg,[64] under specific conditions where Coriolis coupling is considered, multiple Q branches may overlap, resulting in a narrow peak at the band center. A corresponding simulated profile is displayed in Figure 3f, which aligns well with the observed spectrum shown in Figure 3c. Experimental band centers were taken as the peak positions for type-A and type-C bands, and the dip positions for the type-B bands. The integrated area within the shadow region was taken as the intensity of each band. The uncertainties for the band intensities were estimated to be about 5% and could be much larger for overlapping or weak bands.

Regional Analysis. Figures 4–9 show the comparison between experimental and calculated spectra in different frequency ranges. The experimental amplitudes were normalized according to the sample pressure, intracavity laser power, and exposure time. Different band types ("A", "B", "C") were indicated in Figures 4–9 with red, blue, and green arrows, respectively. The calculated amplitudes were normalized relative to the ν_5 band intensity. Calculated bands with different symmetries, a_{1g}, e_g, and a_{1g} + e_g, are highlighted in orange, purple, and gray colors in the bottom panels of Figures 4–9. Although anharmonic effects have been incorporated in the calculation, the current theoretical accuracy remains insufficient to resolve individual substrate contributions within the vibrational manifold. To address this limitation, we adopt the following approach: the total intensity of an overtone or combination band manifold (mostly noted as a_{1g} + e_g) is represented by the cumulative sum of all Raman-active sub-band intensities, while the manifold's center frequency is determined by the intensity-weighted center of its constituent sub-bands.

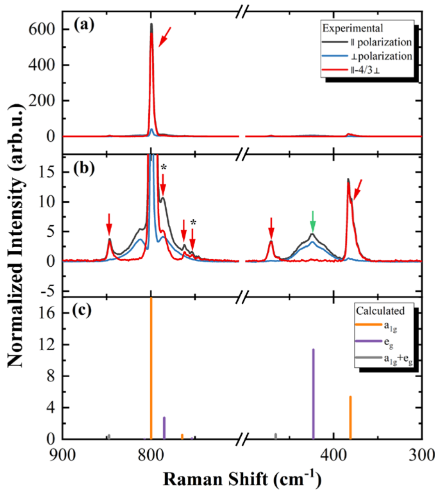

Figure 4. Polarized Raman spectrum of cyclohexane in the range of 300−900 cm^{-1}. (a) Experimental spectrum. Black and blue curves indicate the parallel and perpendicular polarization components, respectively. The red curve shows the extracted polarized component according to eq 2. (b) Enlarged view of the baseline region. Band centers are marked with red, blue, and green arrows, representing type-A, B, and C bands, respectively. (c) Stick spectrum of the calculated Raman bands. Different colors represent band symmetries: a_{1g} (orange), e_g (purple), and a_{1g} + e_g (gray).

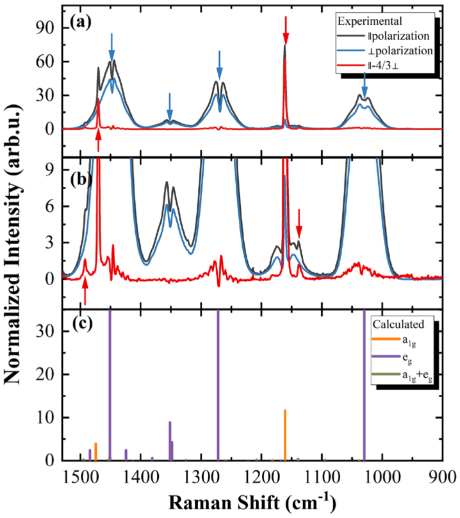

Figure 5. Polarized Raman spectrum of cyclohexane in the range of 900−1500 cm^{-1}. (a) Experimental spectrum. Black and blue curves indicate the parallel and perpendicular polarization components, respectively. The red curve shows the extracted polarized component according to eq 2. (b) Enlarged view of the baseline region. (c) Stick spectrum of the calculated Raman bands.

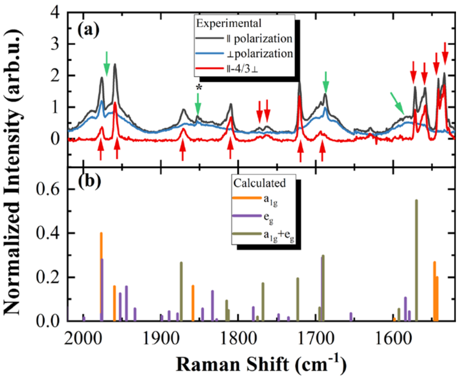

Figure 6. Polarized Raman spectrum of cyclohexane in the range of 1500−2020 cm^{-1}. (a) Experimental spectrum. Black and blue curves indicate the parallel and perpendicular polarization components, respectively. The red curve shows the extracted polarized component according to eq 2. (b) Stick spectrum of the calculated Raman bands.

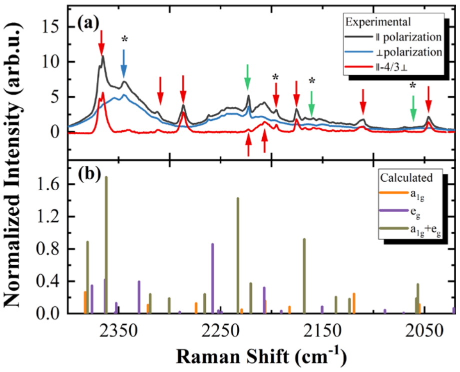

Figure 7. Polarized Raman spectrum of cyclohexane in the range of 2020−2400 cm^{-1}. (a) Experimental spectrum. Black and blue curves indicate the parallel and perpendicular polarization components, respectively. The red curve shows the extracted polarized component according to eq 2. (b) Stick spectrum of the calculated Raman bands.

In total, we confirmed the presence of 71 bands with different symmetries based on the experimental spectra. The positions and integrated intensities of these bands are listed in Tables 1 and 2. Band assignments were conducted by referencing the calculated band positions and intensities, as given in Table S2 of SI and the last two columns of Table 1. Note that the intensity of the ν_5 band has been intensively investigated.[65,66] For convenience, we normalized each band intensity value to a percentage relative to the ν_5 band at 799 cm^{-1}.

300–1500 cm^{-1}. Figures 4 and 5 show the polarized Raman spectra observed in the 300–900 and 900–1500 cm^{-1} regions, respectively. This range includes fundamental bands corresponding to the scissors, rocking, and twisting motions of CH_2 groups, as well as C–C motions.

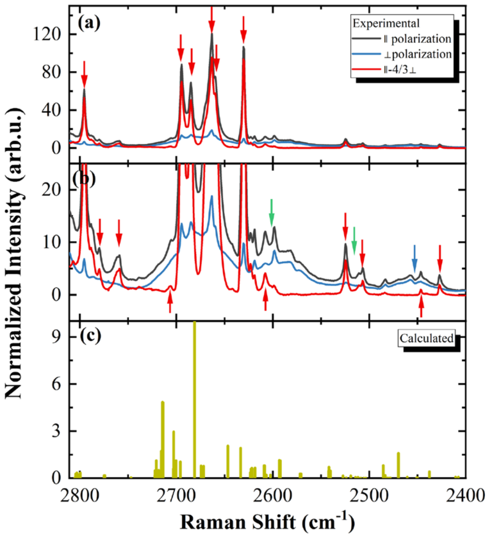

Figure 8. Polarized Raman spectrum of cyclohexane in the range of 2400−2800 cm^{-1}. (a) Experimental spectrum. Black and blue curves indicate the parallel and perpendicular polarization components, respectively. The red curve shows the extracted polarized component according to eq 2. (b) Enlarged view of the baseline region. (c) Stick spectrum of the calculated Raman bands. Note that no symmetry is given here due to high state density.

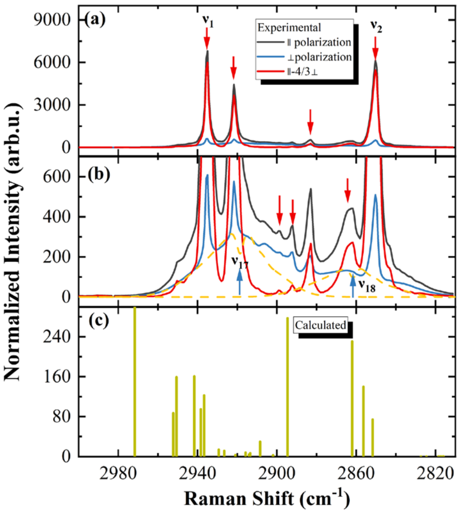

Figure 9. Polarized Raman spectrum of cyclohexane in the range of 2800−3000 cm^{-1}. (a) Experimental spectrum. Black and blue curves indicate the parallel and perpendicular polarization components, respectively. The red curve shows the extracted polarized component according to eq 2. (b) Enlarged view of the baseline region. The yellow dashed lines indicate the profiles of ν_{17} and ν_{18} bands. (c) Stick spectrum of the calculated Raman bands. Note that no symmetry is given here due to high state density.

The fundamental bands ν_3−ν_6 and ν_{19}−ν_{24} can be readily assigned according to calculated results and previous vibrational studies.[44,47,67] The a_{1g} bands ν_6 (384 cm^{-1}), ν_5 (799 cm^{-1}), ν_4 (1161 cm^{-1}), and ν_3 (1470 cm^{-1}) have narrow line widths around 4 cm^{-1} and depolarization ratios close to zero. The strong ν_5 band at 799 cm^{-1} was used as the reference intensity, set at 100%. The fundamental bands with e_g symmetry, ν_{24} (424 cm^{-1}), ν_{22} (1031 cm^{-1}), ν_{21} (1268 cm^{-1}), ν_{20} (1351 cm^{-1}), and ν_{19} (1447 cm^{-1}), exhibit broader profiles, typically spanning 30 cm^{-1}, with a depolarization ratio close to 0.75 and lower amplitudes in the center compared to the a_{1g} bands. The position of the ν_{23} (e_g) band was calculated to be around 785 cm^{-1}. But we could not identify this band, since it overlaps with the rotational structure of the strong ν_5 band at 799 cm^{-1}.

In addition to the fundamental bands given above, several weak bands in this region were observed and assigned to overtone and combination bands involving infrared-active e_u modes ν_{32} (238 cm^{-1}), ν_{30} (906 cm^{-1}) and ν_{29} (1261 cm^{-1}), in line with previous infrared studies.[47,67] Polarized type-A bands at 471, 762 and 847 cm^{-1} were assigned to the overtone bands of $2\nu_{32}$ ($a_{1g} + e_g$), $2\nu_6$ (a_{1g}), and $2\nu_{24}$ ($a_{1g} + e_g$), respectively. As shown in Figure 4, a weak polarized type-A band at 753 cm^{-1} was detected but not matched with calculated results. On the shoulder of the ν_5 band, a type-A band at 787 cm^{-1} probably comes from the $^{13}C^{12}C_5H_{12}$ isotopologue. Taking into account the abundance of $^{13}C/C$ of about 1%, the abundance of $^{13}C^{12}C_5H_{12}$ reaches about 6% in a natural sample of cyclohexane. Vibrational modes of $^{13}C^{12}C_5H_{12}$ were calculated at both the harmonic level and anharmonic level and the spectrum is shown in the Supporting Information (Figure S5). Most of the $^{13}C^{12}C_5H_{12}$ bands overlap with nearby strong bands of the main isotopologue. The $^{13}C^{12}C_5H_{12}$ band with the calculated position of 780 cm^{-1} separates from the narrow ν_5 band of $^{12}C_6H_{12}$ and coincides with the unassigned type-A band observed at 787 cm^{-1}. As shown in Figure 5, narrow type-A bands at 1137 and 1492 cm^{-1} were attributed to combination bands $\nu_{30} + \nu_{32}$ ($a_{1g} + e_g$) and $\nu_{30} + \nu_{32}$ ($a_{1g} + e_g$), respectively. The combination band $\nu_8 + \nu_{32}$ (e_g) has a calculated position of 1348.4 cm^{-1}, which may contribute to the type-B band observed at 1351 cm^{-1} together with the fundamental band ν_{20} (e_g). These observations align well with the calculated values in Table 1.

1500–2400 cm^{-1}. There are no fundamental bands in the region of 1500−2400 cm^{-1}, but by increasing the integrating time to 50 s, we observed several weak bands. Figures 6 and 7 show the polarized Raman spectra in the regions of 1500−2020 and 2020−2400 cm^{-1}, respectively. Comparison of the polarized spectra revealed 21 narrow type-A bands, 1 broad type-B band, and 7 type-C bands in this region, marked with red, blue, and green arrows, respectively. These observations align well with the calculated values in Table 1.

The lower panel of Figure 6 shows the calculated bands, which align well with the experimental data. In the 1500−1600 cm^{-1} range, four type-A bands were observed. According to the calculated results, we tentatively attributed them to combination bands $\nu_4 + \nu_6$ (a_{1g}), $\nu_{15} + \nu_{16}$ (a_{1g}), and the overtone band $2\nu_{23}$ ($a_{1g} + e_g$). The type-C band observed at 1576 cm^{-1} was assigned to the combination band $\nu_4 + \nu_{24}$ (e_g). A prominent depolarized band observed at 1688 cm^{-1} was assigned to the combination band $\nu_{14} + \nu_{32}$ (e_g). The polarized component near this band shows two narrow type-A bands at 1693 cm^{-1} and 1721 cm^{-1}, assigned to the combination band $\nu_{27} + \nu_{32}$ ($a_{1g} + e_g$) and the overtone band $2\nu_{31}$ ($a_{1g} + e_g$), respectively. Their depolarized components are too weak to be detected. The combination band $\nu_{21} + \nu_{24}$ ($a_{1g} + e_g$) may also contribute to the peak at 1693 cm^{-1}.

Four polarized bands and one depolarized band were identified at 1762, 1773, 1810, 1871, and 1852 cm^{-1}, respectively. Calculations place the combination band $\nu_{30} + \nu_{31}$ around 1768 cm^{-1}, $\nu_{20} + \nu_{24}$ around 1775 cm^{-1} and $2\nu_{30}/\nu_{22} + \nu_{23}$ around 1814 cm^{-1}. Another possible candidate is the $\nu_{19} + \nu_{24}$ band with a calculated position near 1873 cm^{-1}.

Table 1. Observed Raman Bands of Cyclohexane and Assignments[a,b,c]

experimental					calculated		
type	ν (cm^{-1})	$I_\perp$	$I_\parallel$	ρ^{exp}	band (sym.)	ν (cm^{-1})	I
A	384	0.163	3.29	0.05	$\nu_6\ (a_{1g})$	380.9	5.35
C	424	4.13	5.51	0.75	$\nu_{24}\ (e_g)$	423.0	11.3
A	471	0	0.806	0	$2\nu_{32}\ (a_{1g} + e_g)$	465.8	0.634
A	753	0	0.202	0	*	*	*
A	762	0	0.264	0	$2\nu_6\ (a_{1g})$	764.5	0.553
A	787	0	1.94	0	*	*	*
A	799	6.00	100	0.06	$\nu_5\ (a_{1g})$	799.6	100
A	847	0	0.504	0	$2\nu_{24}\ (a_{1g} + e_g)$	847.5	0.504
B	1031	36.9	49.2	0.75	$\nu_{22}\ (e_g)$	1029.8	58.2
A	1137	0	0.182	0	$\nu_{30} + \nu_{32}\ (a_{1g} + e_g)$	1139.5	0.384
A	1161	0	9.29	0	$\nu_4\ (a_{1g})$	1161.1	11.6
B	1268	43.7	58.2	0.75	$\nu_{21}\ (e_g)$	1271.9	57.0
B	1351	7.38	9.84	0.75	$\nu_8 + \nu_{32}\ (e_g)$	1348.4	4.29
					$/\nu_{20}\ (e_g)$	1351.5	8.84
B	1447	68.9	91.9	0.75	$\nu_{19}\ (e_g)$	1451.1	76.6
A	1470	0	3.09	0	$\nu_3\ (a_{1g})$	1474.4	3.91
A	1492	0	0.274	0	$\nu_{29} + \nu_{32}\ (a_{1g} + e_g)$	1494.8	0.240
A	1535	0	0.515	0	$\nu_4 + \nu_6\ (a_{1g})$	1543.1	0.199
A	1542	0	0.155	0	$\nu_{15} + \nu_{16}\ (a_{1g})$	1546.3	0.267
A	1560	0	0.322	0	$2\nu_{23}\ (a_{1g} + e_g)$	1569.8	0.548
A	1572	0	0.116	0	*	*	*
C	1576	0.554	0.740	0.75	$\nu_4 + \nu_{24}\ (e_g)$	1584.0	0.106
C	1688	0.922	1.23	0.75	$\nu_{14} + \nu_{32}\ (e_g)$	1691.3	0.288
A	1693	0	0.116	0	$\nu_{27} + \nu_{32}\ (a_{1g} + e_g)$	1690.4	0.297
					$/\nu_{21} + \nu_{24}\ (a_{1g} + e_g)$	1694.9	0.061
A	1721	0	0.236	0	$2\nu_{31}\ (a_{1g} + e_g)$	1723.1	0.194
A	1762	0	0.050	0	$\nu_{30} + \nu_{31}\ (a_{1g} + e_g)$	1768.1	0.171
A	1773	0	0.041	0	$\nu_{20} + \nu_{24}\ (a_{1g} + e_g)$	1775.1	0.021
A	1810	0	0.927	0	$2\nu_{30}\ (a_{1g} + e_g)$	1812.7	0.049
					$/\nu_{22} + \nu_{23}\ (a_{1g} + e_g)$	1814.8	0.092
C	1852	0.760	1.01	0.75	*	*	*
A	1871	0	0.112	0	$\nu_{19} + \nu_{24}\ (a_{1g} + e_g)$	1873.5	0.265
A	1959	0	0.221	0	$\nu_4 + \nu_5\ (a_{1g})$	1959.7	0.158
C	1970	1.10	1.46	0.75	$\nu_{16} + \nu_{27}\ (e_g)$	1975.8	0.279
A	1977	0	0.081	0	$\nu_{14} + \nu_{16}\ (a_{1g})$	1976.7	0.399
A	2046	0	0.298	0	$2\nu_{15}\ (a_{1g})$	2055.2	0.110
C	2048	0.194	0.258	0.75	$\nu_{21} + \nu_{23}\ (a_{1g} + e_g)$	2056.6	0.361
					$/2\nu_{22}\ (a_{1g} + e_g)$	2058.0	0.185
A	2112	0	0.233	0	$2\nu_{11}\ (a_{1g})$	2119.2	0.242
C	2155	1.29	1.72	0.75	*	*	*
A	2175	0	0.271	0	$\nu_{29} + \nu_{30}\ (a_{1g} + e_g)$	2168.0	0.916
A	2195	0	0.186	0	*	*	*
A	2207	0	0.411	0	$\nu_8 + \nu_9\ (a_{1g})$	2206.4	0.156
A	2222	0	0.039	0	$2\nu_8\ (a_{1g})$	2229.4	0.047
C	2228	5.10	6.80	0.75	*	*	*
A	2287	0	0.694	0	$\nu_3 + \nu_5\ (a_{1g})$	2274.2	0.124
A	2312	0	0.066	0	$\nu_{27} + \nu_{31}\ (a_{1g} + e_g)$	2319.1	0.237
					$/2\nu_4\ (a_{1g})$	2321.4	0.105
B	2348	7.94	10.6	0.75	*	*	*
A	2368	0	1.84	0	$\nu_{27} + \nu_{30}\ (a_{1g} + e_g)$	2362.3	1.685

[a] The band type, "A", "B", or "C", is labeled according to the band profile observed in the spectrum. [b] Bands marked with "*" indicate tentative assignments. The calculated band marked with "/" indicates multiple assignments of the same observed band. [c] Both experimental and calculated band intensity values were normalized as a percentage relative to the ν_5 band at 799 cm^{-1}. Experimental band intensities have a relative uncertainty of 5% (1σ), and bands below 2260 cm^{-1} may be attenuated by up to 80% due to the high finesse of the optical cavity. Consequently, relative experimental intensities between distant bands could be distorted.

However, no calculated result matches the observed type-C band at 1852 cm^{-1}. The polarized bands at 1959 and 1977 cm^{-1} were assigned to the combination bands $\nu_4 + \nu_5\ (a_{1g})$ and $\nu_{14} + \nu_{16}\ (a_{1g})$, respectively. The depolarized band observed at 1970 cm^{-1} was assigned to the $\nu_{16} + \nu_{27}\ (e_g)$ band, although its observed intensity is over five times the calculated value. As

Table 2. Observed Raman Bands of Cyclohexane in the Range of 2400−3000 cm^{-1}[a]

type	band (sym.)	ν (cm^{-1})	$I_\perp$	$I_\parallel$	ρ
A		2427	0	0.240	0
A		2446	0	0.085	0
B		2457	2.89	3.86	0.75
A		2509	0	0.880	0
C		2522	1.80	2.39	0.75
A		2524	0	1.11	0
C		2594	12.7	17.0	0.75
A		2608	0	0.450	0
A		2630	0.535	10.7	0.05
A		2660	0.554	13.8	0.04
A		2665	1.25	13.9	0.09
A		2685	0.442	8.87	0.05
A		2694	0.818	11.7	0.07
A		2706	0	0.190	0
A		2759	0	0.546	0
A		2780	0	0.620	0
A		2796	0.500	7.17	0.07
A	ν_2 (a_{1g})	2851	57.0	814	0.07
B	ν_{18} (e_g)	2853	172	229	0.75
A		2862	0	85.9	0
A+C		2884	7.15	29.8	0.24
A+C		2893	2.55	5.76	0.44
A+C		2898	1.13	2.86	0.40
B	ν_{17} (e_g)	2921	470	627	0.75
A		2922	29.1	415	0.07
A	ν_1 (a_{1g})	2935	41.8	597	0.07

[a] Fundamental bands were assigned according to ref 44. Experimental band intensity values were normalized as a percentage relative to the ν_5 band at 799 cm^{-1}.

shown in Figure 7, we observed four depolarized broad features at 2048, 2155, 2228 cm^{-1} with profiles resembling that shown in Figure 3c, and 2348 cm^{-1} with profiles resembling that shown in Figure 3b. By comparing to the calculation and taking into account the symmetry, the band at 2048 cm^{-1} was attributed to bands $\nu_{21} + \nu_{23}$ and $2\nu_{22}$. However, no calculated result matches the bands observed at 2155, 2228, and 2348 cm^{-1}.

The polarized bands observed at 2046, 2112, 2175 and 2195 cm^{-1} have similar intensities, which are tentatively assigned to the $2\nu_{15}$ (a_{1g}), $2\nu_{11}$ (a_{1g}) and $\nu_{29} + \nu_{30}$ ($a_{1g} + e_g$) bands. Likewise, the bands located at 2207, 2222, and 2287 cm^{-1} are assigned to $\nu_8 + \nu_9$ (a_{1g}), $2\nu_8$ (a_{1g}) and $\nu_3 + \nu_5$ (a_{1g}), respectively. But we are unable to give a convincing assignment to the band at 2195 cm^{-1}. For the polarized band observed at 2312 cm^{-1}, we consider two possible assignments: the $\nu_{27} + \nu_{31}$ ($a_{1g} + e_g$) combination band and the $2\nu_4$ (a_{1g}) overtone. The band near 2368 cm^{-1}, which appears as a prominent double peak, is the strongest polarized feature in the region shown in Figure 7. This band is tentatively assigned to the $\nu_{27} + \nu_{30}$ ($a_{1g} + e_g$) band, with the calculated band center near 2362 cm^{-1}.

2400−3000 cm^{-1}. Figures 8 and 9 show the Raman spectra recorded in the range of 2400−3000 cm^{-1}. In the C−H stretching region, four strong fundamental Raman bands are expected:[44,67] ν_2 (2854 cm^{-1}) and ν_1 (2940 cm^{-1}) with a_{1g} symmetry and ν_{18} (2854 cm^{-1}) and ν_{17} (2924 cm^{-1}) with e_g symmetry. Mátrai et al. assigned ν_{18} to a doublet observed at 2888 and 2898 cm^{-1} in the Raman spectrum of liquid cyclohexane. In our spectra, two broad and intense bands with a depolarization ratio of 0.75 are identified at 2853 and 2921 cm^{-1} (orange dashed lines in Figure 9), corresponding to ν_{18} and ν_{17}, respectively. The strong polarized band at 2851 cm^{-1} observed in our spectrum matches the ν_2 (a_{1g}) assignment, being consistent with the analysis by Bernath and Silbert.[44]

Two strong polarized bands were observed at 2922 and 2935 cm^{-1} in our spectra, as shown in Figure 9, which contrasts with the single peak at 2940 cm^{-1} observed in the liquid phase.[67] This observed doublet aligns well with the Hamiltonian model by Bernath and Silbert,[44] predicting two strong a_{1g} bands at 2926.6 and 2943.9 cm^{-1}, due to Fermi coupling between CH stretching and scissor modes.

We also observed many polarized and depolarized bands in this region, and they are marked with arrows in Figures 8 and 9 listed in Table 2. Due to the severe interaction among different vibrational states, it is hard to identify the vibrational quantum numbers for the eigenstates obtained in the calculation. We show the calculated band positions and intensities in Figures 8 and 9 without identifying the symmetries, and we can see a considerable deviation from the observed results. Some observed bands are notably intense, such as the narrow band near 2660 cm^{-1}, indicating that a comprehensive analysis should include overtone and combination bands. Many of these bands remain unassigned due to limitations in current calculations and effective models with reduced vibrational modes.[44]

We can see that the calculation does not agree well with the experimental results in the C−H stretching region. C−H stretching vibrations are well-known for large amplitude motions, which is a challenge for perturbation methods, especially for the cyclohexane molecule with 6 identical C−H stretching modes. Fermi resonances with the bending modes and accidental resonances with other overtone and combination bands considerably complicate the interaction diagram of the vibrations in this region. Therefore, we investigate the low-frequency regions in this work and will extend the analysis to high-frequency regions in the future.

■ CONCLUSIONS

In this study, we present a polarized Raman spectroscopy analysis of cyclohexane using a cavity-enhanced Raman spectrometer with a resolution of approximately 2 cm^{-1}. Polarized Raman spectra of gaseous cyclohexane were recorded at room temperature across a spectral range of 200−3200 cm^{-1}. The high sensitivity and resolution of the spectrometer enabled us to identify about 80 bands, with intensities spanning over 4 orders of magnitude. Through analysis of the polarized and depolarized components, we determined the positions, intensities, and depolarization ratios of these bands, subsequently assigning the bands by comparison with DFT calculations and force field models.

Gas-phase measurements allowed for the resolution of bands that overlap in the condensed phase. Notably, we identified a double peak in the prominent ν_1 band, which was previously observed as a single peak in liquid-phase Raman spectra. The narrow, polarized bands in the gas-phase Raman spectra offered significant advantages for vibrational analysis, enabling us to identify a few tens combination and overtone bands for the first time. Most combination and overtone bands below 2400 cm^{-1} were successfully assigned through comparison of experimental and calculated data. Our analysis highlights the necessity of accounting for anharmonicity and right resonances analysis when modeling vibrational modes, especially for the combinations and overtones. However, the complexity of these bands presents challenges in reliably assigning bands in the high-frequency region. New simulation models are required to be developed in the future, to account for the enhanced magnetic and electric field more precisely due to the confined cavity.

As cyclohexane serves as a model molecule, the methodology developed in this work can be extended to other molecules. For many compounds, vibrational spectra are available only for liquid-phase samples due to sensitivity limitations, while most vibrational studies rely on single-molecule calculations that align more closely with gas-phase properties. Sensitive Raman analysis of gaseous molecules thus provides a valuable link, bridging these studies and clarifying interactions among different vibrational modes. Comparisons with new experimental observations from advanced techniques can provide valuable insights for improving both molecular structure calculations and spectra simulation methods. Such experimental data can guide the development of more accurate and efficient theoretical approaches, bridging the gap between theory and experiment. We anticipate broad applications of this approach across various fields.

■ ASSOCIATED CONTENT

SI Supporting Information

The Supporting Information is available free of charge at https://pubs.acs.org/doi/10.1021/acs.jpca.4c07709.

Vibrational modes of cyclohexane (chair conform): normal mode structures, displacement vectors, and anharmonic modes after variational corrections (PDF)

■ AUTHOR INFORMATION

Corresponding Authors

Yan Tan − *Hefei National Laboratory, University of Science and Technology of China, Hefei 230088, China;* orcid.org/0000-0003-3073-3152; Email: tanyan@ustc.edu.cn

Shui-Ming Hu − *Hefei National Research Center of Physical Sciences at the Microscale, University of Science and Technology of China, Hefei 230026, China; Hefei National Laboratory, University of Science and Technology of China, Hefei 230088, China;* orcid.org/0000-0002-1565-8468; Email: smhu@ustc.edu.cn

Authors

Qing-Ying Yang − *Hefei National Research Center of Physical Sciences at the Microscale, University of Science and Technology of China, Hefei 230026, China*

Qin Yang − *Institute of Organic Chemistry and Biochemistry, Czech Academy of Science, Prague 16610, Czechia*

Yi-Fan Song − *State Key Laboratory of Molecular Reaction Dynamics, Department of Chemical Physics, University of Science and Technology of China, Hefei 230026, China*

An-Wen Liu − *State Key Laboratory of Molecular Reaction Dynamics, Department of Chemical Physics, University of Science and Technology of China, Hefei 230026, China; Hefei National Laboratory, University of Science and Technology of China, Hefei 230088, China;* orcid.org/0000-0001-9835-3530

Jin Wang − *Hefei National Research Center of Physical Sciences at the Microscale, University of Science and Technology of China, Hefei 230026, China*

Yu R. Sun − *Institute of Advanced Science Facilities, Shenzhen 518107, China*

Complete contact information is available at: https://pubs.acs.org/10.1021/acs.jpca.4c07709

Author Contributions

#Q.-Y.Y. and Q.Y. are contributed equally to this work.

Notes

The authors declare no competing financial interest.

■ ACKNOWLEDGMENTS

This work was jointly supported by the Ministry of Science and Technology of China (Grant No. 2022YFF0606500), the National Natural Science Foundation of China (Grant Nos. 22273096, 12393822, and 12393825), and the Innovation Program for Quantum Science and Technology (Grant Nos. 2021ZD0303304 and 2023ZD0301000). Q.Y. acknowledges the EU's Horizon Europe programme MSCA (No. 101107213) and EU-COST Action (CA21101). Prof. Julien Bloino is also acknowledged for the discussion and locally modified version of Gaussian on anharmonic simulation. S.M.H. acknowledges suggestions from Dr. Xiaogang Wang. Computational resources were provided by the e-INFRA Czech project (ID:90254) and Scuola Normale Superiore (Pisa, IT).

■ REFERENCES

(1) Guo, S.; Popp, J.; Bocklitz, T. Chemometric analysis in Raman spectroscopy from experimental design to machine learning-based modeling. *Nat. Protoc.* **2021**, *16*, 5426−5459.

(2) Virga, A.; Ferrante, C.; Batignani, G.; Fazio, D. D.; Nunn, A. D.; Ferrari, A. C.; Cerullo, G.; Scopigno, T. Coherent anti-Stokes Raman spectroscopy of single and multi-layer graphene. *Nat. Commun.* **2019**, *10*, 3658.

(3) Moreau, J.; Rinnert, E. Fast identification and quantification of BTEX coupling by Raman spectrometry and chemometrics. *Analyst* **2015**, *140*, 3535−3542.

(4) Sharma, S. K.; Misra, A. K.; Sharma, B. Portable remote Raman system for monitoring hydrocarbon, gas hydrates and explosives in the environment. *Spectrochim. Acta A Mol. Biomol. Spectrosc.* **2005**, *61*, 2404−2412.

(5) Kharbach, M.; Mansouri, M. A.; Taabouz, M.; Yu, H. Current Application of Advancing Spectroscopy Techniques in Food Analysis: Data Handling with Chemometric Approaches. *Foods* **2023**, *12*, 2753.

(6) Takahashi, T.; Takahagi, W.; Tasumi, E.; Makabe, A.; Taguchi, K.; Thornton, B.; Takai, K. In Situ Measurement of Liquid and Gas CO_2 with High Purity at Deep-Sea Hydrothermal Vents in the Mariana Arc Using Raman Spectroscopy. *ACS Earth & Space Chem.* **2023**, *7*, 2489−2497.

(7) Sharma, S. K.; Porter, J. N.; Misra, A. K.; Acosta-Maeda, T. E.; Angel, S. M.; McKay, C. P. Standoff Raman spectroscopy for future Europa Lander missions. *J. Raman Spectrosc.* **2020**, *51*, 1782−1793.

(8) Hao, R.; Zhao, J.; Liu, J.; You, H.; Fang, J. Remote Raman Detection of Trace Explosives by Laser Beam Focusing and Plasmonic Spray Enhancement Methods. *Anal. Chem.* **2022**, *94*, 11230−11237.

(9) Ren, W.; Wang, B.; Xie, Z.; Wang, H.; Zhu, X.; Zhao, W. An Unmanned Vehicle-Based Remote Raman System for Real-Time Trace Detection and Identification. *Photonics* **2023**, *10*, 1230.

(10) Acosta-Maeda, T. E.; Misra, A. K.; Muzangwa, L. G.; Berlanga, G.; Muchow, D.; Porter, J.; Sharma, S. K. Remote Raman measurements of minerals, organics, and inorganics at 430 nm range. *Appl. Opt.* **2016**, *55*, 10283−10289.

(11) Blacksberg, J.; Alerstam, E.; Maruyama, Y.; Cochrane, C. J.; Rossman, G. R. Miniaturized time-resolved Raman spectrometer for planetary science based on a fast single photon avalanche diode detector array. *Appl. Opt.* **2016**, *55*, 739−748.

(12) Mattioda, A. L.; Gavilan, L.; Ricketts, C. L.; Najeeb, P. K.; Ricca, A.; Boersma, C. The NASA Raman spectroscopic database: Ramdb version 1.00. *Icarus* **2024**, *408*, No. 115769.

(13) Mendili, Y. E.; Vaitkus, A.; Merkys, A.; Gražulis, S.; Chateigner, D.; Mathevet, F.; Gascoin, S.; Petit, S.; Bardeau, J. F.; Zanatta, M.; et al. Raman Open Database: first interconnected Raman-X-ray diffraction open-access resource for material identification. *J. Appl. Crystallogr.* **2019**, *52*, 618−625.

(14) Okada, H.; Sanders, S. T. First-order prediction of the relative performance of infrared (IR) absorption, Raman, and combined (IR + Raman) spectroscopy for estimating composition and bulk properties of fuel mixtures. *IEEE Sens. J.* **2022**, *22*, 16046−16054.

(15) Postnikov, A.; Majtyka-Piłat, A.; Chrobak, D.; Deniszczyk, J. Calculated vibration spectrum of calcium hexahydroxodizincate dihydrate (qatranaite). *Spectrochim. Acta A Mol. Biomol. Spectrosc.* **2024**, *318*, No. 124414.

(16) Lindenmaier, R.; Scharko, N. K.; Tonkyn, R. G.; Nguyen, K. T.; Williams, S. D.; Johnson, T. J. Improved assignments of the vibrational fundamental modes of ortho-, meta-, and para-xylene using gas- and liquid-phase infrared and Raman spectra combined with ab initio calculations: Quantitative gas-phase infrared spectra for detection. *J. Mol. Struct.* **2017**, *1149*, 332−351.

(17) Guirgis, G. A.; Nielsen, C. J.; Horn, A.; Aleksa, V.; Klaeboe, P. Infrared and Raman spectra, DFT-calculations and spectral assignments of silacyclohexane. *J. Mol. Struct.* **2012**, *1023*, 189−196.

(18) Keefe, C. D.; Pickup, J. E. Infrared optical constants, dielectric constants, molar polarizabilities, transition moments, dipole moment derivatives and Raman spectrum of liquid cyclohexane. *Spectrochim. Acta A Mol. Biomol. Spectrosc.* **2009**, *72*, 947−953.

(19) Verma, P.; Truhlar, D. G. Status and challenges of density functional theory. *Tren. Chem.* **2020**, *2*, 302−318.

(20) Cohen, A. J.; Mori-Sánchez, P.; Yang, W. Challenges for density functional theory. *Chem. Rev.* **2012**, *112*, 289−320.

(21) Xu, R.; Jiang, Z.; Yang, Q.; Bloino, J.; Biczysko, M. Harmonic and anharmonic vibrational computations for biomolecular building blocks: Benchmarking DFT and basis sets by theoretical and experimental IR spectrum of glycine conformers. *J. Comput. Chem.* **2024**, *45*, 1846−1869.

(22) Puzzarini, C.; Bloino, J.; Tasinato, N.; Barone, V. Accuracy and Interpretability: The Devil and the Holy Grail. New Routes across Old Boundaries in Computational Spectroscopy. *Chem. Rev.* **2019**, *119*, 8131−8191.

(23) Pele, L.; Šebek, J.; Potma, E. O.; Gerber, R. B. Raman and IR spectra of butane: Anharmonic calculations and interpretation of room temperature spectra. *Chem. Phys. Lett.* **2011**, *515*, 7−12.

(24) Zhang, S.; Jia, H.; Song, M.; Shen, H.; Dongfei, L.; Haibo, L. Raman spectroscopy study of acetonitrile at low temperature. *Spectrochim. Acta A Mol. Biomol. Spectrosc.* **2021**, *246*, No. 119065.

(25) Rullich, C. C.; Kiefer, J. Enantioselective Raman spectroscopy (esR) for distinguishing between the enantiomers of 2-butanol. *Analyst* **2018**, *143*, 3040−3048.

(26) Kessler, J.; Bour, P. Classical trajectory of molecules in electromagnetic field: A handy method to simulate molecular vibrational spectra. *J. Chem. Theory Comput.h* **2022**, *18*, 1780−1787.

(27) Varandas, A. J. C. Scale-free-modeling (harmonic) vibrational frequencies: Assessing accuracy and cost-effectiveness by CBS extrapolation. *J. Chem. Phys.* **2022**, *157*, 174110.

(28) Ye, K.; Wang, S.; Huang, Y.; Hu, M.; Zhou, D.; Luo, Y.; Ye, S.; Zhang, G.; Jiang, J. Machine Learning Prediction of Molecular Binding Profiles on Metal-Porphyrin via Spectroscopic Descriptors. *J. Phys. Chem. Lett.* **2022**, *15*, 1956−1961.

(29) Zou, Z.; Zhang, Y.; Liang, L.; Wei, M.; Leng, J.; Jiang, J.; Luo, Y.; Hu, W. A deep learning model for predicting selected organic molecular spectra. *Nat. Comput. Sci.* **2023**, *3*, 957−964.

(30) Wang, Z.; Pakoulev, A.; Dlott, D. D. Watching vibrational energy transfer in liquids with atomic spatial resolution. *Science* **2002**, *296*, 2201−2203.

(31) Hamada, K.; Ozin, G. A.; Robinson, E. A. The Raman spectra of the chlorofluorosilanes in the gaseous, liquid, and solid state; Anomalous ^{35}Cl, ^{37}Cl isotope intensity effects in the splitting of the totally symmetrical SiCl stretching mode in $SiCl_3F$ and $SiCl_2F_2$. *Can. J. Chem.* **1971**, *49*, 477−480.

(32) Hippler, M. Cavity-enhanced Raman spectroscopy of natural gas with optical feedback cw-diode lasers. *Anal. Chem.* **2015**, *87*, 7803−7809.

(33) Petrov, D.; Matrosov, I. Natural gas analysis using polarized Raman spectroscopy. *Anal. Chem.* **2023**, *95*, 9409−9414.

(34) Wang, P.; Chen, W.; Wang, J.; Lu, Y.; Tang, Z.; Tan, Y. Cavity-enhanced Raman spectroscopy for detection of trace gaseous impurities in hydrogen for fuel cells. *Anal. Chem.* **2023**, *95*, 6894−6904.

(35) Merian, A.; Silva, A.; Wolf, S.; Frosch, T.; Frosch, T. Ultrasensitive Raman gas spectroscopy for dinitrogen sensing at the parts-per-billion level. *Anal. Chem.* **2024**, *96*, 14884−14890.

(36) Wang, P.; Chen, W.; Wang, J.; Zhou, F.; Hu, J.; Zhang, Z.; Wan, F. Hazardous Gas Detection by Cavity-Enhanced Raman Spectroscopy for Environmental Safety Monitoring. *Anal. Chem.* **2021**, *93*, 15474−15481.

(37) Yang, Q. Y.; Tan, Y.; Qu, Z. H.; Sun, Y.; Liu, A. W.; Hu, S. M. Multiple gas detection by cavity-enhanced Raman spectroscopy with sub-ppm sensitivity. *Anal. Chem.* **2023**, *95*, 5652−5660.

(38) Xu, B.; Mao, N.; Zhao, Y.; Tong, L.; Zhang, J. Polarized Raman Spectroscopy for Determining Crystallographic Orientation of Low-Dimensional Materials. *J. Phys. Chem. Lett.* **2021**, *12*, 7442−7452.

(39) Kiefer, J.; Noack, K. Universal enantioselective discrimination by Raman spectroscopy. *Analyst* **2015**, *140*, 1787−1790.

(40) Ossikovski, R.; Picardi, G.; Ndong, G.; Chaigneau, M. Raman spectroscopy and polarization: Selected case studies. *C. R. Phys.* **2012**, *13*, 837−852.

(41) Luo, Y. Chemistry in the Era of Artificial Intelligence. *Precis. Chem.* **2023**, *1*, 127−128.

(42) Raj, A.; Kato, C.; Witek, H. A.; Hamaguchi, H. O. Toward standardization of Raman spectroscopy: Accurate wavenumber and intensity calibration using rotational Raman spectra of H_2, HD, D_2, and vibration-rotation spectrum of O_2. *J. Raman Spectrosc.* **2020**, *51*, 2066−2082.

(43) Itoh, N. Reliable estimation of wavenumbers for peaks of benzonitrile and cyclohexane. *J. Raman Spectrosc.* **2023**, *54*, 113−123.

(44) Bernath, P. F.; Sibert, E. L. Cyclohexane vibrations: High-resolution spectra and anharmonic local mode calculations. *J. Phys. Chem. A* **2020**, *124*, 9991−10000.

(45) Miller, F. A.; Golob, H. R. The infrared and Raman spectra of cyclohexane and cyclohexane-d12. *Spectrochim. Acta* **1964**, *20*, 1517−1530.

(46) Dows, D. A. Normal vibrations of cyclohexane. Infrared spectrum of the crystall. *J. Mol. Spectrosc.* **1965**, *16*, 302−308.

(47) Wiberg, K. B.; Shrake, A. A vibrational study of cyclohexane and some of its isotopic derivatives-III. A vibrational analysis of cyclohexane, cyclohexane-d12, cyclohexane-1,1,4,4-d4 and cyclohexane-1,1,2,2,4,4,5,5-d8. *Spectrochim. Acta, Part A* **1973**, *29*, 583−594.

(48) Durig, J. R.; Zheng, C.; Defrawy, A. M. E.; Ward, R. M.; Gounev, T. K.; Ravindranathb, K.; Rao, N. R. On the relative intensities of the Raman active fundamentals, r_0 structural parameters, and pathway of chair-boat interconversion of cyclohexane and cyclohexane-d_{12}. *J. Raman Spectrosc.* **2009**, *40*, 197−204.

(49) Lorenzo, C. F.; Alcantara, R.; Martin, J. Raman intensities of cyclohexane in the gas phase. *J. Raman Spectrosc.* **1989**, *20*, 291−296.

(50) Fenner, W. R.; Hyatt, H. A.; Kellam, J. M.; Porto, S. P. S. Raman cross section of some simple gases. *J. Opt. Soc. Am.* **1973**, *63*, 73−77.

(51) Mátrai, E.; Császár, P.; Fogarasi, G.; Gál, M. Scaled quantum mechanical (SQM) force field and vibrational assignment for cyclohexane. *Spectrochim. Acta, Part A* **1985**, *41*, 425−433.

(52) Yang, Q.; Mendolicchio, M.; Barone, V.; Bloino, J. Accuracy and reliability in the simulation of vibrational spectra: A comprehensive benchmark of energies and intensities issuing from

generalized vibrational perturbation theory to second order (GVPT2). *Front. Astro. Space Sci.* **2021**, *8*, No. 665232.

(53) Santra, G.; Sylvetsky, N.; Martin, J. M. L. Minimally Empirical Double-Hybrid Functionals Trained against the GMTKN55 Database: revDSD-PBEP86-D4, revDOD-PBE-D4, and DOD-SCAN-D4. *J. Phys. Chem. A* **2019**, *123*, 5129−5143.

(54) Barone, V. Anharmonic vibrational properties by a fully automated second-order perturbative approach. *J. Chem. Phys.* **2005**, *122*, No. 014108.

(55) Bloino, J.; Biczysko, M.; Barone, V. General perturbative approach for spectroscopy, thermodynamics, and kinetics: Methodological background and benchmark studies. *J. Chem. Theory Comput.h* **2012**, *8*, 1015−1036.

(56) Papajak, E.; Zheng, J.; Xu, X.; Leverentz, H. R.; Truhlar, D. G. Perspectives on basis sets beautiful: Seasonal plantings of diffuse basis functions. *J. Chem. Theory Comput.h* **2011**, *7*, 3027−3034.

(57) Papajak, E.; Truhlar, D. G. Convergent partially augmented basis sets for post-hartree- fock calculations of molecular properties and reaction barrier heights. *J. Chem. Theory Comput.h* **2011**, *7*, 10−18.

(58) Duschinsky, F. On the interpretation of electronic spectra of polyatomic molecules. I. Concerning the Franck-Condon principle. *Acta Physicochim. URSS* **1937**, *7*, 551−566.

(59) Baiardi, A.; Bloino, J.; Barone, V. General time dependent approach to vibronic spectroscopy including Franck−Condon, Herzberg−Teller, and Duschinsky effects. *J. Chem. Theory Comput.h* **2013**, *9*, 4097−4115.

(60) Small, G. J. Herzberg−Teller vibronic coupling and the Duschinsky effect. *J. Chem. Phys.* **1971**, *54*, 3300−3306.

(61) Bloino, J. A VPT2 route to near-infrared spectroscopy: The role of mechanical and electrical anharmonicity. *J. Phys. Chem. A* **2015**, *119*, 5269−5287.

(62) Barone, V.; Biczysko, M.; Bloino, J. Fully anharmonic IR and Raman spectra of medium-size molecular systems: accuracy and interpretation. *Phys. Chem. Chem. Phys.* **2014**, *16*, 1759−1787.

(63) Yang, Q.; Bloino, J. An effective and automated processing of resonances in vibrational perturbation theory applied to spectroscopy. *J. Phys. Chem. A* **2022**, *126*, 9276−9302.

(64) Herzberg, G. *Molecular spectra and molecular structure. Vol. II: Infrared and Raman spectra of polyatomic molecules*; Van Nostrand, Reinhold: New York, 1945.

(65) Raj, A.; Witek, H. A.; Hamaguchi, H. O. Determination of accurate absolute Raman cross-sections of benzene and cyclohexane in the gas phase. *Asian J. Phys.* **2021**, *30*, 321−335.

(66) Trulson, M. O.; Mathies, R. A. Raman cross section measurements in the visible and ultraviolet using an integrating cavity: Application to benzene, cyclohexane, and cacodylate. *J. Chem. Phys.* **1986**, *84*, 2068−2074.

(67) Mátrai, E.; Gál, M.; Keresztury, G. Interpretation of the CH stretching region of the vibrational spectra of cyclohexane. *Spectrochim. Acta, Part A* **1990**, *46*, 29−32.

https://doi.org/10.1021/acs.jpca.4c07709
J. Phys. Chem. A 2025, 129, 3183−3193